The Journal of Chemical Physics

RESEARCH ARTICLE | OCTOBER 23 2023

Effect of wall free energy formulation on the wetting phenomenon: Conservative Allen–Cahn model

Hongmin Zhang ; Yanchen Wu ; Fei Wang ; Britta Nestler

J. Chem. Phys. 159, 164701 (2023)
https://doi.org/10.1063/5.0168394

AIP Publishing

The Journal of Chemical Physics ARTICLE pubs.aip.org/aip/jcp

Effect of wall free energy formulation on the wetting phenomenon: Conservative Allen–Cahn model

Cite as: J. Chem. Phys. 159, 164701 (2023); doi: 10.1063/5.0168394
Submitted: 18 July 2023 • Accepted: 4 October 2023 •
Published Online: 23 October 2023

Hongmin Zhang,[1,2] Yanchen Wu,[1,2] Fei Wang,[1,2,a)] and Britta Nestler[1,2,3]

AFFILIATIONS

[1] Institute for Applied Materials–Microstructure Modelling and Simulation (IAM-MMS), Karlsruhe Institute of Technology (KIT), Straße am Forum 7, Karlsruhe 76131, Germany
[2] Institute of Nanotechnology, Karlsruhe Institute of Technology, Hermann-von-Helmholtz Pl. 1, 76344 Eggenstein-Leopoldshafen, Germany
[3] Institute of Digital Materials Science (IDM), Karlsruhe University of Applied Sciences, Moltkestraße 30, Karlsruhe 76133, Germany

[a)] **Author to whom correspondence should be addressed:** fei.wang@kit.edu

ABSTRACT

Cahn introduced the concept of wall energy to describe the interaction between two immiscible fluids and a solid wall [J. W. Cahn, J. Chem. Phys. **66**, 3667–3672 (1977)]. This quintessential concept has been successfully applied to describe various wetting phenomena of a droplet in contact with a solid surface. The usually formulated wall free energy results in the so-called surface composition that is not equal to the bulk composition. This composition difference leads to a limited range of contact angles which can be achieved by the linear/high-order polynomial wall free energy. To address this issue and to improve the adaptability of the model, we symmetrically discuss the formulation of the wall free energy on the Young's contact angle via Allen–Cahn model. In our model, we modify the calculation of the fluid-solid interfacial tensions according to the Cahn's theory by considering the excess free energy contributed by the distorted composition profile induced by the surface effect. Additionally, we propose a semi-obstacle wall free energy which enforces the surface composition to be the bulk composition within the framework of bulk obstacle potential. By this way, the accuracy of the contact angle close to 0° and 180° is significantly improved in the phase-field simulations. We further reveal that the volume preservation term in the conservative Allen–Cahn model has a more significant impact on the wetting behavior on superhydrophobic surfaces than on hydrophilic surfaces, which is attributed to the curvature effect. Our findings provide alternative insights into wetting behavior on superhydrophilic and superhydrophobic surfaces.

I. INTRODUCTION

When a drop is deposited on a homogeneous solid surface, it spreads over the surface to minimize the total surface energy when there is no phase transformation. At the equilibrium state, the liquid either becomes a spherical cap with a finite contact angle or forms a thin film on the surface, which is called as partial wetting and complete wetting, respectively. The static wetting state of a droplet on a homogeneous surface is well described by Young's law. However, the dynamic wetting process is influenced by various factors, including the surface tensions, viscosity, chemical composition, and the roughness of the solid surface. Understanding the wetting behavior is crucial for many industrial applications, such as high-performance coatings,[1,2] electrochemical energy systems,[3,4] functional devices and surfaces,[5,6] and catalyst surfaces treatment.[7]

The investigation of dynamic wetting phenomena is highly interdisciplinary which involves physical chemistry, statistical physics, thermodynamics, and fluid dynamics.[8,9] To study the complex dynamic wetting phenomenon, theoretical and numerical methods have been widely conducted. The theoretical methods can be divided into two principal categories, namely molecular kinetic

theory in the microscopic level[10] and hydrodynamic theory in the macroscopic scale.[11] Due to the rapid development of computing resources in recent years, numerous numerical methods have been implemented to investigate the wetting phenomena.[12] Typical methods are the volume-of-fluid (VOF),[13] the level-set (LS),[14] the front-tracking (FT),[15] lattice-Boltzmann (LB),[16–18] and phase-field (PF)[19] methods. Among these methods, different wetting boundary conditions (WBCs) have been constructed. The typically used WBCs include two forms: surface energy form and geometric form. The former one is based on Cahn's theory in terms of the surface free energy.[20] Herein, the surface free energy has two contributions. The first contribution comes from the appearance of the composition gradient due to the distortion of the concentration profile;[21] the second contribution is the interaction between the fluids and the solid wall due to direct contact. The second contribution is also called wall free energy, denoted as Γ_s. Despite the general form of Cahn,[22] de Gennes[8] expands Γ_s as a power series with respect to the surface composition ϕ_s. Based on previous works, Jacqmin[19] described the wall free energy Γ_s in the form of

$$\int_S f_w(\phi_s) dS, \tag{1}$$

which is adopted in this work. Here, S represents the solid substrate within the spatial domain Ω, and ϕ_s is the surface composition. The integrand $f_w(\phi_s)$ denotes the wall free energy density and describes the interfacial tension in the vicinity of the contact line. Based on these ideas, many early studies employed the formulation of the wall free energy density $f_w(\phi_s)$ with linear form,[16–18] cubic form,[23–31] and high-order polynomial form.[32–34] In contrast to the direct application of the expansion form,[35,36] Jacqmin[19] implemented the microscale contact angle as a prescribed simulation parameter into $f_w(\phi_s)$, which facilitates the efficient study for wetting behavior. Here, we denote the prescribed contact angle as θ (Young's contact angle) and the contact angle from simulation as θ_{sim}. As revealed by Qian *et al.*[37] and Ding and Spelt,[38] there exist non-neglected deviations between the simulated and prescribed contact angles. Ding *et al.* proposed a geometric form which is strictly derived from the geometry in the vicinity of the contact line. As proved by Ding and Spelt,[38] the geometric wetting boundary condition (WBC) can be transformed into the surface energy form. Liang *et al.*[30] found that the geometric form is unstable when the static contact angle is beyond the range $(20°, 160°)$. In the present work, we will systematically investigate how the formulation of the wall energy density influences the wetting behaviour in the diffuse interface model. In our previous work,[39] the simulation results reveal that the surface composition significantly influences the wetting behavior by introducing additional energetic contributions, known as the surface excess energy. This finding implies that the interfacial tension is comprised of both the wall free energy and the excess surface energy, when the surface composition deviates from the bulk value. Without considering the latter part leads to deviations between the prescribed and simulated contact angles. Building upon this work, we further investigate the modification for the theoretical calculation of contact angles with the WBC via high-order polynomial wall energy density.[33] In the current paper, different formulations of wall free energy density will be applied to the WBCs; numerical simulations based on the conservative Allen–Cahn model, which is a specialized PF model utilizing the antiforcing free energy term to ensure volume conservation,[40] will be performed to confirm the theoretical calculations. However, it is worth emphasizing that the conclusions in terms of WBCs presented in this study are applicable to other diffuse interface models, provided that the fundamental concept of wall free energy proposed by Cahn[22] is embraced.

Table I lists the related articles in recent years discussing the wall free energy density with different forms. Qian *et al.*[37] introduced uncompensated Young stress into the WBC to address the deviations between prescribed and simulated contact angles. As Ding and Spelt[38] pointed out, this method mitigates the deviations and the problem is not able to be fully solved. Later on, Wiklund *et al.*[28] pointed out that the linear form introduces a nonphysical film and proposed a cubic form to eliminate this nonphysical layer. In this approach, the concentration profile in the vicinity of the contact line is theoretically solved and is substituted into the WBC so that the wall energy density is obtained. The elimination of the nonphysical layer via the cubic wall energy density has also been noticed by Connington and Lee[36] However, extending the cubic wall energy density to a more general principle for different bulk free energy densities remains an unsolved issue. Moreover, the applied wall energy density is not implemented with prescribed contact angle θ as the input

TABLE I. Summary of recent works for the wall energy density forms.

Authors (publication year)	$f_w(\phi_s)$ forms	Input parameter(s) for θ_{sim}
Qian *et al.* (2006)[37]	Sinusoidal form	$\cos\theta$
Wiklund *et al.* (2011)[28]	Cubic form	$\cos\theta$
Connington and Lee (2013)[36]	Cubic form	...[a]
Ben Said *et al.* (2014)[32]	High-order polynomial form	γ_{ls} and γ_{gs}
Huang *et al.* (2015)[41]	Linear, cubic and sinusoidal forms	$\cos\theta$ and ϕ_s
Liang *et al.* (2019)[30]	Linear and cubic forms	$\cos\theta$
Yue (2020)[31]	Cubic form	$\cos\theta$
Huang *et al.* (2022)[42]	Hyperbolic tangent form	$\cos\theta$, K_{EOS} and K_{INT}
Oktasendra *et al.* (2023)[34]	High-order polynomial form	$\mu_{lr}(\mathbf{r})$[b] or $\cos\theta$[c]

[a]Giving coefficients, which do not prescribe contact angle.
[b]For long-range interactions.
[c]For short-range interactions.

parameter. In fact, as will be shown in the current work, the appearance of the nonphysical layer comes from the deviation of surface composition from the bulk value. We will elucidate the construction of the wall free energy density for different bulk free energy densities. We adopt a straightforward and universally applicable principle to ensure that the surface composition equals to the bulk value and avoid the nonphysical layer. Huang *et al.*[41] systematically compared the performance of linear, cubic, and sinusoidal wall energy density forms in terms of static and dynamic contact angles. However, when the prescribed contact angle θ is not equal to 90°, the implementation of WBCs in this article requires explicitly calculating the surface composition ϕ_s as an input parameter. Noteworthily, the calculation of ϕ_s in Ref. 41 is achieved by assuming a quadratic function of ϕ_s in the normal direction of the wall, which is purely a numerical treatment. This numerical treatment significantly differs from the present work.

Liang *et al.*[30] compared the performance of the geometric and cubic energy forms for the static and dynamic contact angles. They found that the geometric form is unstable on the superhydrophilic substrates and that the cubic form, while performing better for the static contact angle on superhydrophilic substrates, is not as good as the geometric form for dynamic contact angles near 180°. In 2020, Yue[31] proposed a cubic form with prescribed microscale contact angle θ, which is derived by substituting the equilibrium bulk profile of the phase-field parameter into the natural boundary condition. More importantly, this form is proved to satisfy a dissipative energy law. The present concept of the semi-obstacle wall free energy is similar to Yue's work, where the surface composition effect is eliminated. In contrast to the double-well potential in Yue's work, an obstacle potential is employed in the current work, which can significantly save the computational time. Another difference is that we adopt two prescribed parameters as input parameters in the model, namely the interfacial tension parameters between fluids and solid, γ_{ls} and γ_{gs}, to give the prescribed contact angle. Utilizing this method, we can achieve the simulated contact angle close to 0° and 180°. As Yue pointed out that the other wall energy density forms[37,43,44] may result in the distortions of concentration profile, we will discuss in detail from the physical perspective in the present work. In 2022, Huang *et al.*[42] reformulated the wall energy density function as a hyperbolic tangent form with two independent parameters K_{EOS} and K_{INT}. By adjusting these two parameters, the shape of the wall energy density is changed, leading to surface compositions close to the bulk values. As a result, the deviations between the surface composition and the bulk value can be dramatically reduced. However, as will demonstrated in the following, the same effect can be achieved in our proposed wall energy density without introducing additional independent parameters. In 2023, Oktasendra *et al.*[34] introduced the long-range interactions between liquid and solid surfaces into the WBC and discussed its influence on wetting behaviors for partial wetting, complete wetting, and pseudo-partial wetting scenarios. When specifically considering the influence of short-range interactions, a quadratic form of the wall free energy density is employed. Although they demonstrated better accuracy in terms of prescribed contact angle θ and simulated contact angle θ_{sim} compared to the explicitly given ϕ_s methods with linear/cubic forms,[41,45] they did not discuss the impact of surface composition on the static contact angle. The superiority of the quadratic form over other forms arises from its ability to ensure that the surface compositions equal to bulk values for the given bulk free energy density.

All the aforementioned boundary conditions yield nearly identical results when the static contact angle is around between 50° and 130°. For dynamic wetting processes, the scope of the contact angles is reduced. Larger deviations between simulated and prescribed contact angles can be observed for superhydrophilic (with $\theta \lesssim 30°$) and superhydrophobic (with $\theta \gtrsim 150°$) substrates. The primary cause for the deviations can be attributed to the presence of surface composition ϕ_s, which exists either beneath the droplet or at the interface of the gas and solid, denoted as ϕ_{s_1} and ϕ_{s_0}, respectively (cf. Fig. 1). When using these WBCs to address wetting problems on superhydrophobic/superhydrophilic substrates, a modification of the prescribed interfacial tension parameters for liquid-solid and gas-solid is essentially required according to the theory of Cahn. Without the modification by considering the additional excess free energy, it is difficult to accurately and directly reproduce a contact angle close to 0° or 180°. Herein, we systematically study different formulations of the wall free energy density by considering the surface composition and the related excess free energy. In addition, we propose a new wall energy density in the form of semi-obstacle to enforce the order parameter to be the bulk values. By this way, we eliminate the surface composition effect. This allows us to improve the performance of simulating the wetting phenomenon on superhydrophobic/superhydrophilic substrates. Specifically, we focus on discussing the accuracy of different typical wall energy density forms for superhydrophilic and superhydrophobic wetting conditions, and demonstrate the validity and robustness of the modified WBCs.

The rest of the paper is organized as follows. In Sec. II, the PF model with Allen–Cahn type and the three typical wall free energy density forms will be described and discussed. In Sec. III, the respective simulated results of surface compositions and static contact angles for different wall energy formulations in WBCs are presented, the analytical solutions with or without the contribution of the volume-preservation term f_{vp} are compared, and the effect of the initial droplet shapes is discussed. The conclusion is given in Sec. IV.

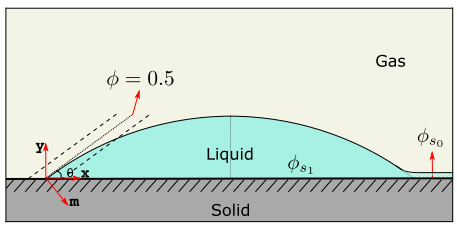

FIG. 1. Schematic of the diffuse interface model: a liquid drop deposited on a solid substrate. The surface compositions ϕ_s vary within the range of [0, 1]. Specifically, ϕ_{s_1} and ϕ_{s_0} denote the equilibrium surface composition beneath the droplet and at the interface of gas-solid, respectively. **m** is the normal vector of the liquid-gas interface.

II. NUMERICAL MODEL

A. Allen–Cahn model and liquid-gas surface tension

We consider a system consisting of two immiscible fluids in contact with a solid flat substrate. The volume-preserved Allen–Cahn model is applied to simulate the equilibrated droplet on a solid substrate with the Young's contact angle of θ. In our model, we introduce an order parameter ϕ to characterize the phase state. In particular, the states $\phi = 0$ and 1 stand for the pure gas and pure liquid phase, respectively. By this way, the physical interpretation of the order parameter ϕ could be the local volume fraction of the liquid phase. Inside the gas-liquid interface, the order parameter ϕ varies gradually between 0 and 1. Denoting the fluid domain by Ω, the free energy functional of the system reads

$$\Psi(\phi) = \int_{\Omega}\left[\frac{\gamma_{lg}}{\epsilon}w(\phi) + \epsilon\gamma_{lg}|\nabla\phi|^2 + f_{vp}(\phi)\right]d\Omega, \tag{2}$$

where ϵ is related to the width of the diffuse interface. The selection criterion for the interface width and its ratio to the droplet size is shown in the supplementary material document. The bulk energy density $w(\phi)$ is described by the obstacle potential as

$$w(\phi) = \begin{cases} \frac{16}{\pi^2}\phi(1-\phi) & \text{if } 0 \le \phi \le 1 \\ +\infty & \text{otherwise.} \end{cases} \tag{3}$$

When the value of ϕ is less than 0 or exceeds 1, it is reset to 0 or 1, respectively, due to the infinite energy barrier. The infinite energy barrier is motivated by the infinite entropy of pure materials. This physically motivated numerical technique significantly reduces the computational overhead in comparison with the hyperbolic tangent interface profile when using double well potential. The term $\epsilon\gamma_{lg}|\nabla\phi|^2$ denotes the gradient energy density. The third term f_{vp} ensures the volume preservation of the droplet and is expressed as[40]

$$f_{vp}(\phi) = \chi_1 g(\phi) + \chi_2[1 - g(\phi)], \tag{4}$$

where $g(\phi)$ is an interpolation function, expressed as $g(\phi) = \phi^3(6\phi^2 - 15\phi + 10)$. The weights χ_1 and χ_2 are interpreted as the partial pressure of the liquid and the gas phases, respectively. More discussions are shown in Ref. 40. As will be discussed in the following, the difference of $\chi_1 - \chi_2$ has a significant influence on the interfacial energy.

According to the hypothesis of van der Waals,[46] the interface profile is obtained by minimizing the free energy functional, Eq. (2). Applying the variational calculus to Ψ, we obtain the chemical potential μ with the following equation:

$$\mu = \frac{\delta\Psi}{\delta\phi} = \frac{\gamma_{lg}}{\epsilon}w'(\phi) - 2\epsilon\gamma_{lg}\nabla^2\phi + f'_{vp}(\phi). \tag{5}$$

Utilizing the steepest descent method to extend the hypothesis as a time-dependent model, we obtain the following governing equation of the system:

$$\tau\epsilon\partial_t\phi = -\frac{\gamma_{lg}}{\epsilon}w'(\phi) + 2\epsilon\gamma_{lg}\nabla^2\phi - f'_{vp}(\phi), \tag{6}$$

where τ is a positive time relaxation coefficient. When the time tends to be large, we have $\partial_t\phi = 0$ and the equilibrium state given by Eq. (5) is replicated. In the present study, our emphasis is on the derivation of the equilibrium contact angle attributed to the surface effect. The impact of τ on the dynamic wetting behavior demands a further meticulous examination, which is out of the scope of the current work. For a more comprehensive understanding on the dynamic wetting and the parameter τ, we refer to Refs. 47 and 48. By setting $\mu = 0$ with the far field condition, we obtain the following equilibrium condition

$$\frac{\gamma_{lg}}{\epsilon}w'(\phi) + f'_{vp}(\phi) = 2\epsilon\gamma_{lg}\nabla^2\phi. \tag{7}$$

In one dimension with zero mean curvature, the contribution of f_{vp} to the energy functional vanishes since the pressure is uniform and can be any arbitrary value as a reference state. In this case, the surface tension of the liquid-gas interface can be analytically obtained as follows. Multiplying by $\frac{\partial\phi}{\partial x}$ in Eq. (7) and integrating from $-\infty$ to x, we obtain

$$\epsilon\gamma_{lg}\left(\frac{\partial\phi}{\partial x}\right)^2 = \frac{\gamma_{lg}}{\epsilon}\Delta w(\phi), \tag{8}$$

where $\Delta w(\phi) = w(\phi) - w(\phi_0) - (\phi - \phi_0)w'(\phi_0) = w(\phi)$ with $w(\phi_0) = 0$, $w'(\phi_0) = 0$ and ϕ_0 standing for the value of ϕ in bulk phases. Here, we define the value in bulk phase as: $\phi_0 = 0$ and $\phi_1 = 1$. A further simplification of Eq. (8) leads to

$$\frac{\partial\phi}{\partial x} = \pm\sqrt{\frac{1}{\epsilon^2}\Delta w(\phi)}. \tag{9}$$

Here, the positive gradient signifies the calculating direction pointing to liquid phase, and vice versa. The fluid-fluid interfacial tension equals to the integration of the excess bulk free energy density through the interface plus the gradient energy density. By this way, the formulation for the surface tension reads[20]

$$\begin{aligned}\sigma &= \int_{-\infty}^{+\infty}\left[\frac{\gamma_{lg}}{\epsilon}\Delta w(\phi) + \epsilon\gamma_{lg}\left(\frac{d\phi}{dx}\right)^2\right]dx \\ &= 2\gamma_{lg}\int_{\phi_0}^{\phi_1}\sqrt{\Delta w(\phi)}d\phi,\end{aligned} \tag{10}$$

where $\int_{-\infty}^{+\infty}dx$ means the integration over the interface from one bulk phase to the other one. As sketched in Fig. 2(b), the integration in the phase-field space is represented by the hatched area for $\gamma_{lg} = 1$.

B. The natural wetting boundary condition

Following the theory of Cahn,[22] the substrate energy is composed of two parts. The first part is the liquid-solid interfacial energies, namely the wall free energy Γ_s. The second contribution arises from the distortions of $\phi(x)$ profile as the order parameter ϕ changes from the bulk compositions ϕ_0/ϕ_1 to the substrate composition ϕ_s, resulting from the joint equilibrium of bulk and substrate, as will be demonstrated in the following. It is important to emphasize that the volume conservative term f_{vp} is deliberately omitted in the substrate energy. This exclusion stems from two key considerations. Firstly, the boundary is treated as a single layer in the current model. Consequently, the consideration of mass conservation becomes unnecessary due to the substantial ratio of the droplet

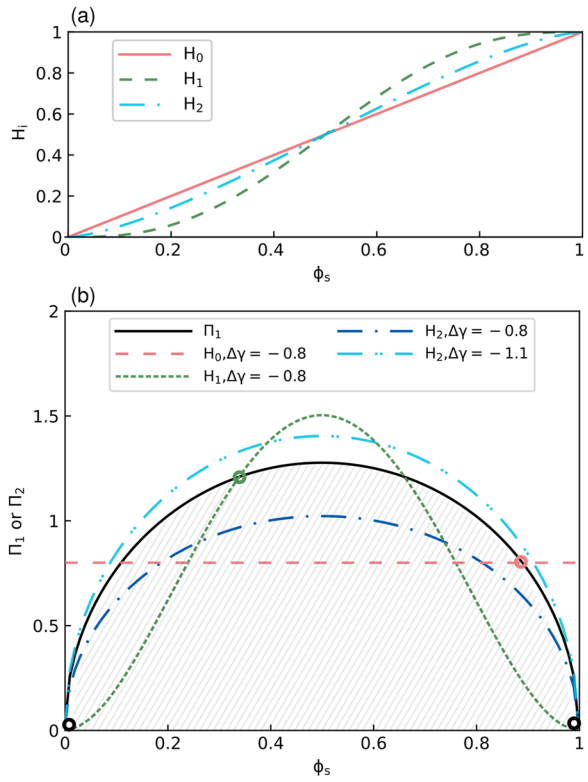

FIG. 2. (a) The graphic description of three typical types of the wall energy function $h(\phi_s)$, namely H_0: linear, H_1: high-order polynomial, and H_2: semi-obstacle. (b) Illustration for the determination of the surface composition given by the intersection of the two curves Π_1 and Π_2, with $\Pi_1 = 2\gamma_{lg}\sqrt{\Delta w(\phi_s)}$, $\Pi_2 = -\Delta\gamma h'(\phi_s)$, and $\Delta\gamma = \gamma_{gs} - \gamma_{ls}$. The intersections between the solid curve Π_1 and non-solid curves Π_2 determine the possible surface compositions ϕ_s. The appropriate solutions of ϕ_{s_1} corresponding to a local energy minimum are highlighted by different colored symbols.

volume to the surface area of the single layer. Secondly, we focus on the static equilibrium, a non-conservative boundary condition without f_{vp} is applicable in line with the treatment of Jacqmin.[19] Thus, the free energy functional at the substrate reads

$$\Psi_s = \int_\Omega \epsilon\gamma_{lg}(\nabla\phi_s)^2 d\Omega + \int_S f_w(\phi_s) dS, \tag{11}$$

where S is the substrate in contact with the fluid phases. The composition ϕ_s denotes the order parameter on the surface. The term $f_w(\phi_s)$ represents the wall free energy density which describes the short-range interaction between the fluids and solid substrate. In accordance with literature,[32,33] the wall free energy density is formulated as

$$f_w(\phi_s) = \gamma_{ls} h(\phi_s) + \gamma_{gs}[1 - h(\phi_s)]. \tag{12}$$

Here, $h(\phi_s)$ is a wall energy density function. γ_{ls} and γ_{gs} are respectively the interfacial tensions of the liquid-solid and gas-solid interfaces. The specific form of $h(\phi_s)$ will be discussed in the following.

The local equilibrium on the substrate requires $\delta\Psi_s/\delta\phi_s = 0$. After transforming the volume integration to the surface integral by using the divergence theorem, we obtain the following equation for the equilibrium condition on the substrate

$$2\epsilon\gamma_{lg}\nabla\phi_s \cdot \mathbf{n} - f'_w(\phi_s) = 0, \tag{13}$$

where $\mathbf{n}$ is the normal vector of the substrate pointing to fluids. When an appropriate wall energy function $h(\phi_s)$ is chosen, the so-called "wall layer"[25] can be avoided and the surface compositions ϕ_s equal to the equilibrium values of bulk phases, namely $\phi_s = 0$ or 1. In this case, the natural boundary condition, Eq. (13) is consistent with Yong's law, and the static contact angle obeys $\cos\theta = (\gamma_{gs} - \gamma_{ls})/\gamma_{lg}$. The derivation is shown in the supplementary material (section: Derivation of Young's law in diffuse interface model). More details can be found in Ref. 49. Therefore, the static contact angle θ can be simply determined by the three interfacial tension parameters, σ (with $\sigma = \gamma_{lg}$), γ_{gs}, and γ_{ls}. However, when the surface compositions ϕ_s deviate from the bulk compositions, the above derivation has to be amended. In this case, the interfacial tensions of the liquid-solid and gas-solid interface have to be modified due to the existence of additional excess energy.[8,22,39] By considering the bulk equilibrium, Eq. (9) and the substrate equilibrium, Eq. (13), the surface composition ϕ_s can be analytically solved as following

$$\pm 2\gamma_{lg}\sqrt{\Delta w(\phi_s)} = f'_w(\phi_s). \tag{14}$$

The sign of − and + indicates hydrophobic and hydrophilic wetting situations, respectively. The intersection of the curve $2\gamma_{lg}\sqrt{\Delta w(\phi_s)}$ with $f'_w(\phi_s)$ leads to two equilibrium surface compositions in the droplet and in the surrounding phase. We use ϕ_{s_1} and ϕ_{s_0} to indicate the equilibrium surface composition beneath and outside of the droplet, respectively (see schematic Fig. 1). The modified interfacial tensions γ^*_{gs} and γ^*_{ls} include the contribution of wall free energy density at the substrate as well as the excess free energy due to the distribution of the non-uniform compositions from the substrate to the bulk phase. Thus, the modified interfacial tensions read

$$\gamma^*_{gs} = f_w(\phi_{s_0}) + 2\gamma_{lg}\int_{\phi_{s_0}}^{0}\sqrt{\Delta w(\phi)}d\phi, \tag{15}$$

$$\gamma^*_{ls} = f_w(\phi_{s_1}) + 2\gamma_{lg}\int_{\phi_{s_1}}^{1}\sqrt{\Delta w(\phi)}d\phi. \tag{16}$$

Applying the solution of Eq. (14) to the above equations, the modified interfacial tensions are obtained. Through linking the modified interfacial tensions to the equilibrium contact angle, we now have the modified contact angle θ^* calculated via $\cos\theta^* = (\gamma^*_{gs} - \gamma^*_{ls})/\gamma_{lg}$ in a closed form. The consistency of the new formulation with the Young's law is derived as follows. Multiplying by $\frac{\partial\phi}{\partial x}$ in Eq. (13) and integrating it across the interface on the substrate, we obtain

$$\int_{-\infty}^{+\infty} 2\epsilon\gamma_{lg}\frac{\partial\phi}{\partial n}\frac{\partial\phi}{\partial x} - \frac{\partial f_w}{\partial\phi}\frac{\partial\phi}{\partial x}dx = 0. \tag{17}$$

Via the definition of integral calculus, the second term can be readily simplified as $\int_{-\infty}^{+\infty}\frac{\partial f_w}{\partial\phi}\frac{\partial\phi}{\partial x}dx = f_w(\phi_{s_1}) - f_w(\phi_{s_0})$. Comparing with the derivation by Xu and Wang,[49] the key modification here is the

first term in Eq. (17). The integration boundary must be changed to ϕ_{s_0} and ϕ_{s_1}. By dividing the new integral boundary into three parts, we obtain the following equation for the first term in Eq. (17)

$$\int_{-\infty}^{+\infty} 2\epsilon\gamma_{lg}\frac{\partial\phi}{\partial n}\frac{\partial\phi}{\partial x}dx = \int_{\phi_{s_0}}^{0} 2\epsilon\gamma_{lg}\frac{\partial\phi}{\partial n}d\phi + \int_{0}^{1} 2\epsilon\gamma_{lg}\frac{\partial\phi}{\partial n}d\phi + \int_{1}^{\phi_{s_1}} 2\epsilon\gamma_{lg}\frac{\partial\phi}{\partial n}d\phi. \quad (18)$$

According to Fig. 1, we have the following geometrical relation $\frac{\partial\phi}{\partial n} = -\frac{\partial\phi}{\partial m}\cos\theta^*$. Substituting this geometrical relation into Eq. (18) and using the definition of γ_{gs}^* and γ_{ls}^* given by Eq. (16), we obtain the following equality

$$\int_{0}^{1} 2\epsilon\gamma_{lg}\frac{\partial\phi}{\partial n}d\phi = \int_{0}^{1} 2\epsilon\gamma_{lg}\frac{\partial\phi}{\partial m}d\phi\cos\theta^* = \gamma_{gs}^* - \gamma_{ls}^*.$$

With the calculation of the surface tension σ of Eq. (10), we achieve the modified Young's equation in terms of the amended interfacial energies as

$$\cos\theta^* = \frac{\gamma_{gs}^* - \gamma_{ls}^*}{\gamma_{lg}}. \quad (19)$$

1. Discussion of the wall energy density function $h(\phi_s)$

In the following discussion, we define $\gamma_{gs} - \gamma_{ls}$ as $\Delta\gamma$ and the derivative of the wall free energy as $\Pi_2 = -\Delta\gamma h'(\phi_s)$. The integrand for the fluid-fluid surface tension is defined as $\Pi_1 = 2\gamma_{lg}\sqrt{\Delta w(\phi_s)}$. As pointed out by de Gennes,[8] any form of the wall energy density function $h(\phi_s)$ in Cahn's approach[22] is deemed acceptable. To accurately describe the van der Waals interaction between liquid and gas and between fluid and solid, the sub-regular solution model with $\sum_{i,j}\chi_{ij}\phi^i(1-\phi)^j + \sum_i\chi_i\phi^i + \sum_j\nu_j(1-\phi)^j$ has often been applied in statistical mechanics.[50,51] The first, second and third term depicts the van der Waals interaction between liquid and gas, liquid and solid, and gas and solid, respectively. Here, the parameters χ_{ij}, χ_i, and ν_j represent the intermolecule potential. In line with the sub-regular solution model, we introduce three typical types of wall energy density function $h(\phi_s)$, namely, H_0: linear, H_1: high-order polynomial, and H_2: semi-obstacle, as shown in Fig. 2(a). Within this context, the different power series indicate distinct van der Waals interactions between the liquid molecules and the solid atoms. We systematically change the value of $\Delta\gamma$ and investigate how the chosen wall energy function affects the wetting contact angles. The advantages and shortcomings for each wall energy function are discussed in the following. Our emphasis is the static contact angles at the equilibrium states while the dynamic effect is out of the scope of the present work.

As shown in Fig. 2(a), the wall energy function $h(\phi_s)$ fulfills $h(\phi_s = 1) = 1$ and $h(\phi_s = 0) = 0$ to ensure $f_w(\phi_s = 1) = \gamma_{ls}$ and $f_w(\phi_s = 0) = \gamma_{gs}$. The choice of $h(\phi_s)$ determines the surface compositions, as graphically illustrated in Fig. 2(b) for different types of $h(\phi_s)$. The intersections between the black solid curve Π_1 [left hand side of Eq. (14)], and the other colored curves Π_2 represent the various solutions of the substrate composition ϕ_s. When $\Delta\gamma = -0.8$, the function $f_w'(\phi_s) = -\Delta\gamma h'(\phi_s)$ for different $h(\phi_s) = H_i$ $(i = 0, 1, 2)$ is indicated by the dashed, dot, and dot dashed curves with different colors.

a. H_0: Linear type.

$$h(\phi_s) = \phi_s. \quad (20)$$

As shown in the Fig. 2(b), when applying $\Delta\gamma = -0.8$ corresponding to a hydrophobic setup, the Π_1 curve (black solid) and the Π_2 curve (red dashed) have two intersection points. The right one is the appropriate solution of ϕ_{s_1} marked with the red circle. The other one corresponds to a higher energy state and is physically unstable. If the curves Π_1 and Π_2 are well-defined and finite out of the phase space range, namely $\phi_s > 1$ and $\phi_s < 0$, we should have another surface composition ϕ_{s_0} out of the interval [0, 1], as demonstrated in Refs. 8 and 20. However, due to the specificity of the obstacle form of the bulk free energy density rather than the double well potential, the solution of ϕ_{s_0} must be 0 to reach a minimum of the surface energy. For the hydrophilic wetting with $\Delta\gamma > 0$, the surface composition is reversed. The minimization of the surface energy leads to $\phi_{s_1} = 1$ and $\phi_{s_0} < 0.5$ corresponding to the left intersection point of Π_1 and Π_2 in Fig. 2(b). In the special case $\Delta\gamma = 0$, we have $\theta = 90°$. When applying H_0 with $|\Delta\gamma| > \max(\Pi_1)$, such as $\Delta\gamma = -1.5$ here, it results in no mathematical solution for ϕ_s on the substrate; this means that there is non intersection between the curve Π_1 and Π_2. In this situation, the model of the WBC is not physically meaningful anymore.

b. H_1: High-order polynomial type.

$$h(\phi_s) = \phi_s^3(6\phi_s^2 - 15\phi_s + 10). \quad (21)$$

When applying $\Delta\gamma = -0.8$ to H_1 wall energy formulation, there exist four possible solutions, as depicted by the four intersection points of the black line and the green dashed line. The appropriate solution of $\phi_{s_1} = 0.37$ (green circle) and $\phi_{s_0} = 0$ (black circle) corresponds to a local minimum of the surface energy (see supplementary material document). Noteworthily, this result is affected by the initial state. In the present work, we firstly adopt a complete circle as the initial droplet state to mimic the down-bottom deposition of a droplet in experiments. When other initial conditions are adopted, the appropriate solution of ϕ_{s_1} equals to 1 and the wall layer is eliminated. For the sake of clarity, when not specified, the simulation results in the present work refer to a complete circular initial state. In Sec. III C, we will present the results with a half circle as the initial state. For superhydrophilic and superhydrophobic substrates, the H_2 form leads to a wall layer, resulting from the surface composition ranging between 0 and 1. In this case, the related interfacial tensions between fluids and solid should be modified according to Eqs. (13) and (16). The modified value $|\Delta\gamma^*| = |\gamma_{gs}^* - \gamma_{ls}^*|$ for H_1 is always smaller than 1, as constrained by the limitation of the excess free energy and the maximum value of the wall energy. However, applying H_1 requires a very large value of the input parameter $|\Delta\gamma|$, such as 100 or more, in order to achieve complete wetting or complete dewetting.

c. H_2: Semi-obstacle type.

$$h(\phi_s) = \frac{2}{\pi}\left[\arcsin\left(\sqrt{\phi_s}\right) + (2\phi_s - 1)\sqrt{\phi_s(1-\phi_s)}\right]. \quad (22)$$

The proposed *semi-obstacle* form satisfies the condition $h'(\phi_s) \sim \kappa\sqrt{\Delta w(\phi_s)}$, where κ is a scaling factor and determines the contact angle. This ensures that the solutions of Eq. (14) are limited to 0 and 1. As shown in Fig. 2(b), the surface composition ϕ_{s_1} for H_2 is either 1 or 0 with $\Delta\gamma = -0.8$ or -1.1, respectively, as indicated by the black circles. As a result, the wall layer along the substrate vanishes and there is no need to modify the interfacial tensions between liquid/gas and solid. However, as the volume-preserved Allen–Cahn model is used in this work, the influence of f_{vp} leads to changes in the concentration profile $\frac{\partial\phi}{\partial n}$ in Eq. (13) and the related ϕ_s may deviate slightly from 0 or 1. Taking this into consideration, the theoretical analysis of the impact of f_{vp} on the wetting behavior will be discussed in the following.

2. Discussion for the influence of $f_{vp}(\phi)$

To obtain a more accurate analytical solution, this section discusses the influence of the volume preserve term $f_{vp}(\phi)$ on the interfacial tensions of fluid-solid interface in the vicinity of the contact line. Although the term $f_{vp}(\phi)$ is not explicitly exhibited in the substrate energy in Eq. (11), it is computed in the bulk domain and thus implicitly affects the composition profile of $\phi(x)$, leading to the changes of gradient term $(\nabla\phi_s)^2$ involved in the substrate energy. Equation (7) is rewritten in the polar coordinate to consider the influence of f_{vp} in 2D domain. Due to the axisymmetric property of this problem, the composition profile can be considered along r in any direction. Thus, the bulk equilibrium condition reads:

$$\frac{\gamma_{lg}}{\epsilon}w'(\phi) + f'_{vp}(\phi) = 2\epsilon\gamma_{lg}\left[\frac{\partial^2\phi}{\partial^2 r} + \frac{1}{r}\frac{\partial\phi}{\partial r}\right]. \tag{23}$$

Multiplying by $\frac{\partial\phi}{\partial r}$ on both sides and integrating from $-\infty$ to r_0, we obtain

$$\epsilon\gamma_{lg}\left(\frac{\partial\phi}{\partial r}\right)^2 + 2\epsilon\gamma_{lg}\int_{-\infty}^{r_0}\frac{1}{r}\left(\frac{\partial\phi}{\partial r}\right)^2 dr = \frac{\gamma_{lg}}{\epsilon}\Delta w(\phi) + \Delta f_{vp}, \tag{24}$$

where r_0 represents any specific location within the domain. The term Δf_{vp} is defined as follows

$$\Delta f_{vp} = \begin{cases} f_{vp}(\phi) - f_{vp}(\phi_0) = \Delta\chi g(\phi); \\ f_{vp}(\phi_1) - f_{vp}(\phi) = \Delta\chi(1 - g(\phi)), \end{cases} \tag{25}$$

with $\Delta\chi = \chi_1 - \chi_2$, $\phi_0 = 0$, and $\phi_1 = 1$. Here, $\Delta\chi g(\phi)$ represents the deviation of $f_{vp}(\phi)$ from the bulk term $f_{vp}(\phi_0)$ on hydrophilic substrate, namely the part between the solid and gas phases outside of the droplet for hydrophilic wetting behavior, and vice versa. Since the 2D profile of $\phi(r)$ is unknown, the term $\int_{-\infty}^{r_0} 2\epsilon\gamma_{lg}\frac{1}{r}(\frac{\partial\phi}{\partial r})^2 dr$ is neglected for simplifying the following analysis. Nevertheless, despite this assumption, the analysis provides a calibrating value to be compared with the numerical simulations.

By equating the derivative of ϕ via comparing Eqs. (13) and (24), we obtain an alternative equation for the surface composition

$$\pm 2\sqrt{\gamma_{lg}^2\Delta w(\phi_s) + \epsilon\gamma_{lg}\Delta f_{vp}(\phi_s)} = f'_w(\phi_s). \tag{26}$$

The difference of Eq. (26) from Eq. (14) is the contribution of the volume preservation term. In this case, the integrand for the excess free energy at the substrate has to be modified. With the notation $\Phi = 2\sqrt{\gamma_{lg}^2\Delta w(\phi_s) + \epsilon\gamma_{lg}\Delta f_{vp}(\phi_s)}$, the modified interfacial tensions by considering the volume preservation term are written as

$$\gamma_{gs}^* = f_w(\phi_{s_0}) + \int_{\phi_{s_0}}^{0}\Phi d\phi, \tag{27}$$

$$\gamma_{ls}^* = f_w(\phi_{s_1}) + \int_{\phi_{s_1}}^{1}\Phi d\phi. \tag{28}$$

Note that although $f_{vp}(\phi)$ does not contribute to the wall free energy, Eq. (11), it implicitly affects the substrate composition at equilibrium via Eq. (26) and thus changes the related interfacial tension, γ_{ls}^* and γ_{gs}^*. To address the effect of the volume preservation term Δf_{vp}, we present an estimation of the weight parameters χ_1 and χ_2. The difference of the coefficient $\Delta\chi$ is expressed in the polar coordinate (see the supplementary material for detailed derivation) as follows

$$\Delta\chi = 2\frac{\int_0^\infty -\frac{\gamma_{lg}}{\epsilon}w'(\phi)dr + 2\epsilon\gamma_{lg}\int_0^\infty\left(\frac{\partial^2\phi}{\partial r^2} + \frac{1}{r}\frac{\partial\phi}{\partial r}\right)dr}{\int_0^\infty g'(\phi)dr}. \tag{29}$$

Multiplying by $\frac{\partial\phi}{\partial r}$ on both sides of Eq. (23) and integrating from $-\infty$ to ∞ yield

$$\Delta\bar{\chi} = \chi_1 - \chi_2 = \int_{-\infty}^{\infty} 2\epsilon\gamma_{lg}\frac{1}{r}\left(\frac{\partial\phi}{\partial r}\right)^2 dr \approx \frac{\sigma}{\bar{r}}. \tag{30}$$

At equilibrium, the radius r can be taken as a constant averaged value $\bar{r}$ of the diffuse interface with $\phi = 0.5$. In this work, we apply a constant positive value $\Delta\bar{\chi}$ to Eq. (25) to obtain the analytical solution for the surface composition ϕ_s in Eq. (26).

III. RESULTS AND DISCUSSION

In this section, simulation results with three different wall energy formulations are compared to theoretical results in terms of surface composition ϕ_s and contact angles. The effect of the volume preservation term f_{vp} and the initial droplet shapes will be elucidated as well.

A. Surface composition

We systematically change the parameter $\Delta\gamma$ and conduct a series of 2D simulations with different formulations for the wall free energy. The surface compositions $\phi_{s,sim}$ are measured when the droplet is at the equilibrium state. The theoretically solved surface compositions with and without the effect of f_{vp} are denoted by ϕ_s^* and ϕ_s, respectively. The former one is obtained via solving Eq. (26), while the latter one is solved via the natural boundary conditions Eq. (14). To ensure conciseness, we adopt the notation of ϕ_{s_1} and ϕ_{s_0} to distinguish the surface compositions beneath and outside the droplet, respectively. Following this way, $\phi_{s_1}^*$ and $\phi_{s_0}^*$ denote the equilibrium composition beneath the droplet and at the interface of gas-solid, respectively. Table II tabulates the surface compositions from simulation and theoretical results for a wide range of $\Delta\gamma$ including superhydrophobic and superhydrophilic surfaces. In general, the theoretical results are well consistent with the simulation results and the maximum absolute deviation is less than

TABLE II. Simulation and analytical results of surface compositions for three different formulations of the wall energy density. The analytical surface compositions with and without the effect of the volume preservation term f_{vp} are denoted as ϕ_s^* and ϕ_s. Specifically, $\phi_{s_1}^*$ and $\phi_{s_0}^*$ denote the equilibrium ϕ_s^* beneath the droplet or at the interface of gas-solid, respectively.[a]

		Hydrophobic						Hydrophilic				
	$\Delta\gamma$	−1.5	−1.1	−1.0	−0.9	−0.4	0.0	0.4	0.9	1.0	1.1	1.5
H_0	$(\phi_{s_1}, \phi_{s_0})_{sim}$	(0, 0)	(0.78, 0)	(0.83, 0)	(0.87, 0)	(0.97, 0)	(1, 0)	(1, 0.03)	(1, 0.13)	(1, 0.17)	(1, 0.23)	(1, 1)
	(ϕ_{s_1}, ϕ_{s_0})	...[b]	(0.75, 0)	(0.81, 0)	(0.85, 0)	(0.97, 0)	(1, 0)	(1, 0.03)	(1, 0.15)	(1, 0.19)	(1, 0.25)	...
	$(\phi_{s_1}^*, \phi_{s_0}^*)$	...	(0.77, 0)	(0.81, 0)	(0.86, 0)	(0.98, 0)	(1, 0)	(1, 0.03)	(1, 0.15)	(1, 0.19)	(1, 0.25)	...
H_1	$(\phi_{s_1}, \phi_{s_0})_{sim}$	(0.19, 0)	(0.26, 0)	(0.28, 0)	(0.31, 0)	(1, 0)	(1, 0)	(1, 0)	(1, 0)	(1, 0.73)	(1, 0.75)	(1, 0.81)
	(ϕ_{s_1}, ϕ_{s_0})	(0.18, 0)	(0.24, 0)	(0.26, 0)	(0.29, 0)	(1, 0)	(1, 0)	(1, 0)	(1, 0)	(1, 0.74)	(1, 0.76)	(1, 0.82)
	$(\phi_{s_1}^*, \phi_{s_0}^*)$	(0.19, 0)	(0.25, 0)	(0.27, 0)	(0.31, 0)	(1, 0)	(1, 0)	(1, 0)	(1, 0)	(1, 0.74)	(1, 0.76)	(1, 0.82)
H_2	$(\phi_{s_1}, \phi_{s_0})_{sim}$	(0.01, 0)	(0.07, 0)	(0.96, 0)	(0.96, 0)	(0.99, 0)	(1, 0)	(1, 0)	(1, 0)	(1, 0)	(1, 1)	(1, 1)
	(ϕ_{s_1}, ϕ_{s_0})	(0, 0)	(0, 0)	(1, 0)[c]	(1, 0)	(1, 0)	(1, 0)	(1, 0)	(1, 0)	(1, 0)	(1, 1)	(1, 1)
	$(\phi_{s_1}^*, \phi_{s_0}^*)$	(0.02, 0)	(0.11, 0)	(1, 0)	(1, 0)	(1, 0)	(1, 0)	(1, 0)	(1, 0)	(1, 0)	(1, 1)	(1, 1)

[a]This labeling convention is applicable to the simulated surface compositions as well, namely $\phi_{s_1,sim}$ and $\phi_{s_0,sim}$. For the sake of brevity, we designate $(\phi_{s_1,sim}, \phi_{s_0,sim})$ as $(\phi_{s_1}, \phi_{s_0})_{sim}$ for the remainder of this manuscript.
[b]... represents the absence of a theoretical solution when $\Delta\gamma = \pm 1.5$.
[c]When $\Delta\gamma = \pm 1$, ϕ_s could be any value in the range of [0, 1].

6.5%. For the linear wall free energy H_0, as $\Delta\gamma$ increases from −1.1 to 1.1, the surface composition beneath the droplet ϕ_{s_1} increases until $\phi_{s_1} = 1$ is achieved. With increasing $\Delta\gamma$, the surface composition ϕ_{s_0} at the surrounding-substrate interface becomes non-zero starting from $\Delta\gamma = 0.4$, and then increases until a complete wetting where the surface composition ϕ_{s_0} equals to the bulk of the droplet, namely $\phi_{s_0} = 1$. Note that for a large absolute value of $\Delta\gamma$ [namely $\Delta\gamma > \max(\Pi_1)$, e.g., $|\Delta\gamma| = 1.5$], the two curves Π_1 and Π_2 do not intersect [see Fig. 2(b)]. In this case, the wetting can only be either complete wetting with $(\phi_{s_1}, \phi_{s_0}) = (1, 1)$ or dewetting with $(\phi_{s_1}, \phi_{s_0}) = (0, 0)$. Therefore, attention should be paid carefully on the interfacial tension parameters when H_0 is utilized. For the H_1 form, there are always at least two intersection points of the curves Π_1 and Π_2 that are physically meaningful to describe the wetting behavior irrespective of the value of $\Delta\gamma$. This is a significant difference of H_1 from H_0. Specifically, the wetting is affected only by the derivative of the wall energy rather than the wall energy itself. The linear form H_0 loses its generality as its derivative is a constant which has no dependence on the phase-field variable. In the case of H_1, for a relatively small value of $|\Delta\gamma|$ ($|\Delta\gamma| \le 0.4$), the solutions for the surface composition are 0 and 1. In this case, no modification to the interfacial tensions between liquid/gas and solid is needed. While for a relatively large value of $|\Delta\gamma|$, one of the solutions for ϕ_s lies between 0 and 1 and the surface composition effect appears. In contrast to the above two wall energy functions H_0 and H_1, H_2 ensures that the surface composition is always identical to the bulk values which are either 0 or 1 (i.e., ϕ_0 or ϕ_1), eliminating the need for modification of the interfacial tensions γ_{gs} and γ_{ls}. In particular, when $|\Delta\gamma| = 1$, the two curves Π_1 and Π_2 overlap exactly with each other, resulting in that the theoretical substrate composition ϕ_s can be any value between 0 and 1. Thus, the application of H_2 should avoid the input parameters with $|\Delta\gamma| = 1$, which corresponds to the case of $\theta = 0^\circ$ or 180°.

Upon a closer examination of the results in Table II for the case of H_2, a small deviation between the simulation and theoretical surface compositions is observed, which is possibly due to the influence of f_{vp}. To understand this deviation, we compare the difference between the simulated surface composition $\phi_{s,sim}$ with analytical surface compositions ϕ_s^* and ϕ_s for different values of $\Delta\gamma$. The surface composition difference is defined as $\Delta\phi_s^* = |\phi_{sim} - \phi_s^*|$ and $\Delta\phi_s = |\phi_{sim} - \phi_s|$, corresponding to the case with and without f_{vp} in the theory, respectively. From Table II, we see that $\Delta\phi_s^*$ is smaller than $\Delta\phi_s$ especially in the hydrophobic situation. This result verifies the validity of our analysis for the effect of f_{vp}. The negligible difference between $\Delta\phi_s^*$ and $\Delta\phi_s$ of hydrophilic area indicates that the influence of f_{vp} is less significant in hydrophilic wetting scenario. This is reasonable, since a greater tendency to spread in the hydrophilic case results in smaller curvature. According to the definition of f_{vp}[40] and the derivation of Eq. (30), the value of f_{vp} is closely related to the curvature of the droplet base. Thus, the volume preservation term f_{vp} plays a relatively minor role in the hydrophilic situation. In the hydrophobic case, the mean curvature of the droplet involving in the volume preservation leads to the deviation of the simulation and the theory.

To provide a clearer visualization of the surface compositions, Fig. 3 shows snapshots for the simulated 2D droplets on hydrophobic and hydrophilic substrates with three different wall energy forms H_0, H_1, and H_2. The color bar at the right side presents the value of the order parameter ranging from 0 to 1. As described in the Table II, when $|\Delta\gamma|$ is greater than a certain threshold, the surface compositions ϕ_s for H_0 and H_1 deviate from 0 or 1, resulting in a wall layer beneath the droplet for a superhydrophobic surface or outside the droplet for a superhydrophilic surface. The wall layers beneath and outside the droplet are exemplarily demonstrated in the top and middle panels of Fig. 3(b). Conversely, by using H_2 in the WBC, the substrate composition ϕ_s is identical to 0 or 1, resulting

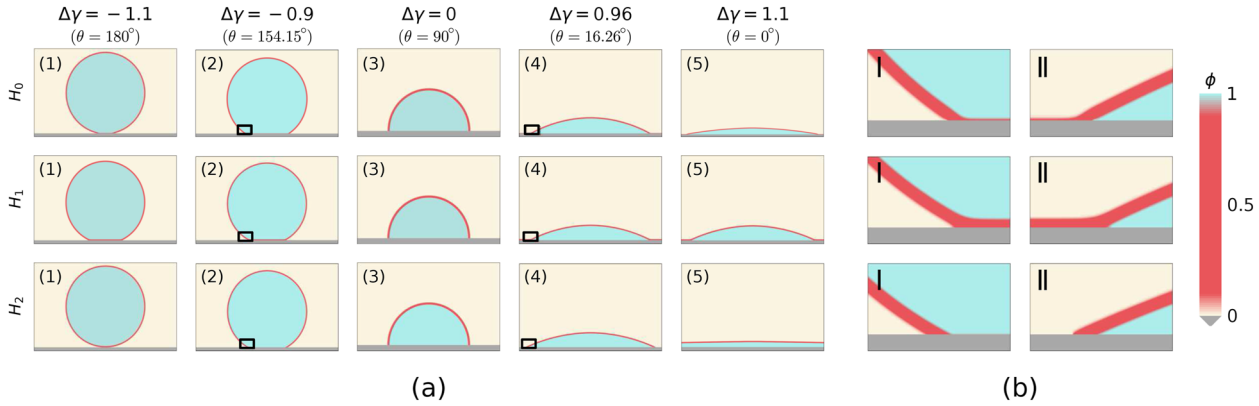

FIG. 3. (a) Simulation results for three different forms of H_i in the wall free energy density: top-H_0; middle-H_1; bottom-H_2. The wettability is varied by varying the parameter $\Delta\gamma$ and θ indicates the expected contact angle. (b) Zoomed-in of the triple junction area illustrating the introduced wall layer for superhydrophobic and superhydrophilic wetting behavior for H_0 and H_1 forms (top and middle panels). The wall layer is avoided by using the H_2 form (bottom panel).

in the absence of the wall layer, as illustrated in the bottom panel of Fig. 3(b).

B. Static contact angle

Next, we present three different measurement criteria for the contact angle, as depicted in Fig. 4. The current methodologies include macroscopic measurement [Fig. 4(a)], semi-macroscopic measurement [Fig. 4(b)], and microscopic measurement [Fig. 4(c)]. Figure 4(a) illustrates the macroscopic contact angle measurement technique. The droplet-gas contour line is defined by the locus of $\phi = 0.5$. Three random points P_0 at the contour line are selected to fit a circle of the cap; the cap radius R and the height H from the circle-center to the substrate are subsequently determined. The contact angle is determined via $\arccos\left(\frac{H}{R}\right)$. Figure 4(b) demonstrates the semi-macroscopic measurement, where the contact angle is defined by $\arctan\left(\frac{H}{L}\right)$. The base radius L is obtained from the triple junction P_1 with the condition of $\phi = \frac{(\phi_{s_1}+\phi_{s_0})_{sim}}{2}$ on the substrate layer. Figure 4(c) presents the microscopic interpretation of the contact angle, where the coordinates of X_1 and X_2 are the contour lines of $\phi = \frac{(\phi_{s_1}+\phi_{s_0})_{sim}}{2}$ in the first (boundary) and of $\phi = 0.5$ in the second layer of the discrete grids, respectively. When the interface point does not coincide with the center of the cell, a linear interpolation is employed to calculate the coordinates. We expect that these three criteria can be applied to experimental graphs as well if ϕ represents the gray scale of the image.

Figure 4(d) depicts the comparison between theoretical and simulation results for contact angle greater than 150° with three different measurements. As an example, the wall energy formulation H_1 is considered here for the comparative study. The solid and dashed lines represent the theoretical results without and with the influence of f_{vp}, denoted as θ^* and $\theta^*_{f_{vp}}$, respectively. The theoretical results are obtained via Eq. (19) with the modified interfacial tensions γ^*_{gs} and γ^*_{ls}. The circle, square, and triangle symbols indicate the PF simulation results corresponding to macroscopic, semi-macroscopic, and microscopic measurements, which are denoted as θ_{sim_0}, θ_{sim_1}, and θ_{sim_2}, respectively. It is observed that the microscopic

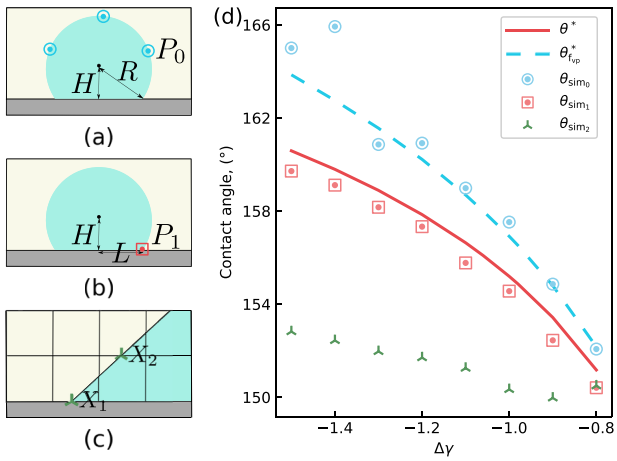

FIG. 4. (a)–(c) Schematics of three different measurements of the contact angle for the simulation results: (a) Macroscopic contact angle via $\theta_{sim_0} = \arccos\left(\frac{H}{R}\right)$. The parameters R and H are determined by fitting a circle of the interface with three random points P_0 given by the locus of $\phi = 0.5$. (b) Semi-macroscopic contact angle $\theta_{sim_1} = \arctan\left(\frac{H}{L}\right)$, where the base radius L is determined by the local interface point P_1 on the substrate with the condition of $\phi = \frac{(\phi_{s_1}+\phi_{s_0})_{sim}}{2}$. (c) Microscopic contact angle via $\theta_{sim_2} = \arctan\left(\frac{1}{X_2 - X_1}\right)$, where X_1 and X_2 are the X-coordinates of the interface points with $\phi = \frac{(\phi_{s_1}+\phi_{s_0})_{sim}}{2}$ and $\phi = 0.5$, respectively. (d) Contact angle as a function of the parameters $\Delta\gamma$ for the wall energy type of H_1. Theoretical results are shown by the dashed and solid lines, denoted as θ^* and $\theta^*_{f_{vp}}$, respectively, with and without the influence of volume preservation term f_{vp}. Simulation results are represented by circles (θ_{sim_0}), squares (θ_{sim_1}), and triangles (θ_{sim_2}) corresponding to the measurements (a)–(c), respectively.

contact angle θ_{sim_2} significantly deviates from the theoretical results. Consequently, in the subsequent discussion, we exclude the microscopic measurement and focus on the other two techniques. The macroscopic and semi-macroscopic methods both provide accurate

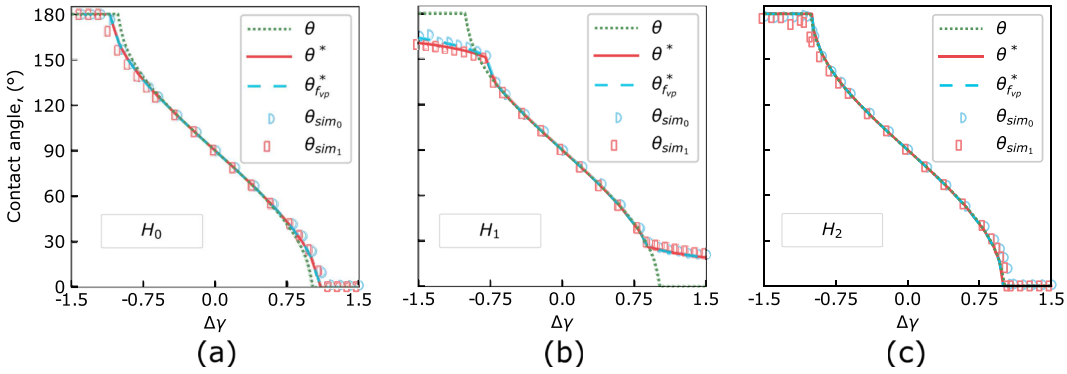

FIG. 5. Comparison of the simulated and theoretical contact angle for three different wall energy forms. Here, $\theta^*_{f_{vp}}$ stands for the theoretical contact angle with the consideration of the influence of the volume preserve term f_{vp}. (a) and (b) are for H_0 and H_1, where the modified Young's law is applied; (c) is for H_2, the wall layer is eliminated.

representations of the contact angle in comparison with the theoretical value. A closer look at Fig. 4(d) shows that the macroscopic contact angle θ_{sim_0} is closer to the theoretical values $\theta^*_{f_{vp}}$ with the effect of f_{vp}. This outcome can be attributed to the fact that the volume preservation term f_{vp} is associated with the redistribution of the mean curvature, resulting in a circular arc at the equilibrium state, which essentially echoes the macroscopic measurement. The semi-macroscopic contact angle θ_{sim_1} shows a better accordance with θ^*, since the consideration of the surface composition can lead to a deviation of the interface from a circular shape in the vicinity of the triple junction.

Figure 5 compares the theoretical and simulation results for the contact angles as a function of $\Delta\gamma$ for three different formulations of the wall free energy. In Figs. 5(a)–5(c), the dotted lines depict the expected contact angle θ calculated through Young's law with $\cos\theta = \frac{\Delta\gamma}{\gamma_{lg}}$. In this case, the interfacial tensions do not include the additional excess energy. The solid and dashed lines represent the theoretical results θ^* and $\theta^*_{f_{vp}}$. The theoretical results are obtained by applying Young's law with the modification of the interfacial tensions γ^*_{gs} and γ^*_{ls} when surface composition appears. The right-half-circle and left-half-square symbols indicate the PF simulation results corresponding to the macroscopic and semi-macroscopic measurements, respectively. Both theoretical contact angles show very good agreement with the simulation results for all three types of the wall free energy. Noteworthily, in Fig. 5(b), the dashed line ($\theta^*_{f_{vp}}$) and solid line (θ^*) display relatively larger deviations when $\Delta\gamma < -0.8$. A magnification of this area has been shown in Fig. 4(d). The difference of $\theta^*_{f_{vp}}$ and θ^* when $\Delta\gamma > 0.8$ is less than that for $\Delta\gamma < -0.8$. This observation demonstrates that f_{vp} plays a more important role on superhydrophobic substrates than on superhydrophilic substrates due to the different mean curvature of the droplet associated with the volume preservation.

It should be noted that in Figs. 5(a) and 5(b), within the range of $\theta \in [50°, 130°]$, the simulation results are well consistent with the unmodified Young's law $\cos\theta = \frac{\Delta\gamma}{\gamma_{lg}}$ and the deviation is less than 2°. We denote the range of $\theta \in [50°, 130°]$ as region I; outside this range is depicted by region II. In I, the desired contact angle can be achieved by directly applying $\Delta\gamma$ since the modification of the interfacial tensions γ_{gs} and γ_{ls} is not needed. In II, the contact angle θ_{sim} from simulation deviates from the expected value calculated through $\cos\theta = \frac{\Delta\gamma}{\gamma_{lg}}$ and the modification of the interfacial tensions γ_{gs} and γ_{ls} is essential. Without the modification, the resulting contact angles (θ_{sim}, θ^*) significantly deviate from θ [see Figs. 5(a) and 5(b)]. The contact angle should be amended as $\cos\theta^* = \frac{\Delta\gamma^*}{\gamma_{lg}}$. For the wall energy formulations with H_0 and H_1, the simulation results θ_{sim_0} exhibit excellent agreement with the theoretical results $\theta^*_{f_{vp}}$ with a deviation less than 3.2°. The best agreement between θ_{sim}, θ, and θ^* is observed for the wall energy formulation with H_2, as demonstrated in Fig. 5(c). The reason is that the excessive free energy at

TABLE III. The difference between the desired θ via Young's law and obtained by simulation θ_{sim} with different wall energy formulations.

		θ_{sim} [b]		
$\Delta\gamma$	θ [a]	H_0	H_1	H_2
−1.50	180.00	180.00	165.01	178.30
−1.10	180.00	176.84	158.99	179.02
−0.98	168.52	156.89	156.4	165.27
−0.90	154.16	147.37	154.86	152.09
−0.80	143.13	138.96	152.07	142.02
−0.60	126.87	125.63	126.6	127.27
−0.40	113.58	113.33	113.45	114.34
0.00	90.00	90.13	89.87	90.21
0.40	66.42	66.93	67.54	66.65
0.60	53.13	55.04	53.80	52.69
0.80	36.87	41.84	38.36	39.34
0.90	25.84	34.03	28.94	30.59
0.96	16.26	28.55	26.60	24.54
1.10	0.00	9.83	24.48	1.20
1.50	0.00	0.97	20.74	0.76

[a] $\cos\theta = \frac{\Delta\gamma}{\gamma_{lg}}$, when $|\Delta\gamma| \geq 1$, considered as complete wetting.

[b] For brevity, we here adopt θ_{sim_0} as simulation results.

the substrate is removed by properly formulating the wall energy density.

Table III illustrates the disparity between the simulated contact angle θ_{sim} and the expected contact angle θ. Significant differences are only observed in II. Although the results for H_0 show good consistency with Young's law, the applicability of H_0 is limited to a specific range of $|\Delta\gamma|$. A large value $[|\Delta\gamma| > \max(\Pi_1)]$ leads to the absence of solutions in Eq. (14) in region II for H_0 wall energy form. The wall energy density with H_1 exhibits the greatest deviation between the desired contact angle θ and θ_{sim} in the complete wetting regions. The complete wetting behavior must be achieved by utilizing a very large value of $|\Delta\gamma|$. The H_2 form demonstrates the highest consistency with Young's law. Directly applying $\Delta\gamma$ into the WBC with H_2 wall energy form can yield a small difference $\Delta\theta = |\theta - \theta_{sim}|$, even in superhydrophobic/superhydrophilic situations. However, it is worth mentioning that when applying H_2 in the WBC, one should avoid the singularity with $|\Delta\gamma| = 1$. As depicted in Table III, except for the point where $|\Delta\gamma| \simeq 1$, the difference $\Delta\theta$ between the desired and simulated contact angles is within 4.8°.

C. Initial states

In this section, we compare simulations initially with a complete circle and a half circle on the substrate. For both initial conditions, the final equilibrium states are most identical except when the H_1 wall energy is applied. As a typical example, the simulation snapshots for H_1 form with $\Delta\gamma = -0.8$ with different initial shapes of droplets are displayed in Fig. 6. The black dashed line in the left panel of Fig. 6 depicts an initial state of a complete circle, leading to the surface composition $\phi_{s_1,sim} = 0.37$, and a contact angle of $\theta_{sim_I} = 150.4°$ at equilibrium state. The black dashed line in the right panel of Fig. 6 illustrates an initial state of a half circle, which results in the surface composition $\phi_{s_1,sim} = 1$ and the contact angle $\theta_{sim_{II}} = 141.4°$ in the final state. In the former case, one has to modify the liquid-solid interfacial tension by taking the surface excess energy into account, leading to the deviation of θ_{sim_I} from θ. In the latter case, there is no need to modify the liquid-solid interfacial tension and the simulation results $\theta_{sim_{II}}$ show good agreement with θ. The noteworthy disparity between θ_{sim_I} and $\theta_{sim_{II}}$ is about 9°, highlighting the sensitivity of the final equilibrium state to the initial shapes of the droplet when the wall free energy formulation of H_1 is applied. The reason for the difference of θ_{sim_I} and $\theta_{sim_{II}}$ is that there are two local minima for the surface energy when applying the H_1 form wall free energy, as depicted in Fig. S3(a) (see supplementary material).

When applying the H_1 form as the WBC for a dynamic wetting process, it is worth to discuss the influence of the initial state and dynamics on the apparent contact angle [see Eq. (17) of Ref. 47]. A change in the equilibrium contact angle will definitely affect the relaxation process towards the equilibrium state. Moreover, within the context of dynamic wetting processes, a slip/wall velocity is often applied to emulate the wetting phenomena, as described in previous studies.[19,47,48] In accordance with Jacqmin's discussion [Eq. (2.16) in Ref. 19], the slip velocity is proportional to the gradient of the wall chemical potential, which is nothing but the variational derivative of the wall free energy with respect to the composition. Therefore, the wall velocity and the associated dynamics are crucially affected by

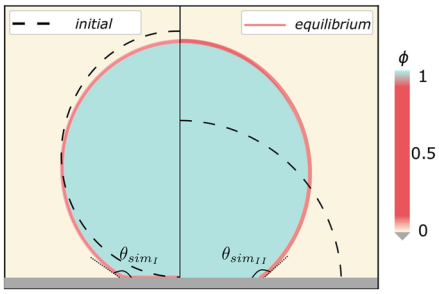

FIG. 6. Simulation results of two distinct initial states for H_1 wall free energy with $\Delta\gamma = -0.8$. Left: the initial droplet is a complete circle; right: the initial droplet is a half circle. The resulting equilibrium contact angles are denoted as θ_{sim_I} and $\theta_{sim_{II}}$. By modifying the initial filling from a complete circle to a half circle, the surface composition transforms from 0.37 to 1, and the equilibrium contact angle changes from 150.4° to 141.4°.

the formulation of the wall free energy and the resulting wall chemical potential. Notably, the utilization of the H_1 form within the WBC allows the surface composition effect, exhibiting distinct characteristics when compared to the wall energy formulations employed in Refs. 19, 47, and 48, where the surface compositions are constrained to match the bulk values. Thus, these corresponding effects on the dynamic wetting process warrant further exploration in future studies.

IV. CONCLUSION

In this work, an Allen–Cahn type phase-field model with three different formulations of wall free energy is used to investigate the equilibrium wetting state of a droplet on a solid substrate. All of the wall energy formulations have an excellent consistency with Young's law within the range of $50° \lesssim \theta \lesssim 130°$. Within this range, we can directly obtain the desired contact angle in accordance with Young's law by applying the input parameter $\Delta\gamma = \gamma_{gs} - \gamma_{lg}$ in simulations. Beyond this range, due to the existence of the surface composition and the associated excess free energy, the parameter $\Delta\gamma$ can not be directly used to calculate the contact angle. Instead, by modifying the interfacial tensions γ_{gs} and γ_{ls}, the contact angle θ^* can be calculated through applying the modified parameter $\gamma^*_{gs} - \gamma^*_{lg}$ to Young's law. It has been proved that simulation results for the contact angles show very good agreement with the theoretical contact angle θ^*. Additionally, we investigate the influences of the volume preserve term f_{vp} of the Allen–Cahn model in wetting scenarios, which is proved to play a significant role in superhydrophobic situations. This conclusion aligns with the definition of f_{vp}, which reflects the curvature effect. For a droplet with the same volume, the equilibrium base radius for superhydrophobic setup is smaller than that for a superhydrophilic surface, so that the influence of f_{vp} is more profound for superhydrophobic setups. The three wall energy forms in WBCs show different advantages and shortcomings. Both H_0 and H_1 allow the existence of surface compositions, therefore, to realize the desired contact angle, the interfacial tensions between solid and liquid/gas (γ_{ls} and γ_{gs}) should be carefully calculated and $\Delta\gamma$ should be accordingly adjusted in the simulation setup. H_2 provides a suitable alternative that aligns well with Young's law results and

avoid the surface composition effect so that no modification to γ_{ls} and γ_{gs} is needed. However, it is worth noting that applying H_2 into the WBC should avoid the singularity point with $\Delta\gamma \simeq 1$. Finally, the evident difference of the equilibrium contact angle for the two different initial states when applying H_1 wall free energy casts light on the contact angle hysteresis. It is worth to further discuss the influences of this form of wall free energy on the contact angle relaxation process during dynamic wetting process by allowing the existence of surface compositions in next steps. To sum up, our investigation in this work discusses the disparity between the commonly used WBCs and the Young's law. Through appropriate modification to the model, a significant increase in the precision of the contact angles in simulations can be achieved. Our work provides essential guidelines for improving the accuracy of modeling of the wetting contact angles for a wide range, especially in superhydrophobic and superhydrophilic situations.

SUPPLEMENTARY MATERIAL

The supplementary material document presents the numerical convergence of the model, the solution of the surface composition, the derivation of Young's law and the parameter $\Delta\chi$ for the diffuse interface model, and a table showing the surface compositions in different WBCs with varying $\Delta\gamma$.

ACKNOWLEDGMENTS

This research was supported by Gottfried-Wilhelm Leibniz prize Grant No. NE 822/31-1 of the German research foundation (DFG), Future Field funding of the KIT excellence strategy of the project "SPPO-Screening Platform for Personalized Oncology," and the VirtMat project "VirtMat P09: Wetting Phenomena" of the Helmholtz association within the MSE Programme No. 43.31.01. The authors acknowledge support by the state of Baden-Württemberg through bwHPC.

AUTHOR DECLARATIONS

Conflict of Interest

The authors have no conflicts to disclose.

Author Contributions

H.Z. and Y.W. contributed equally to this work.

Hongmin Zhang: Conceptualization (equal); Data curation (equal); Formal analysis (equal); Investigation (equal); Methodology (equal); Software (equal); Validation (equal); Visualization (equal); Writing – original draft (equal); Writing – review & editing (equal). **Yanchen Wu**: Conceptualization (equal); Data curation (equal); Investigation (equal); Methodology (equal); Writing – original draft (equal); Writing – review & editing (equal). **Fei Wang**: Conceptualization (equal); Data curation (equal); Formal analysis (equal); Methodology (equal); Software (equal); Supervision (equal); Visualization (equal); Writing – original draft (equal); Writing – review & editing (equal). **Britta Nestler**: Funding acquisition (equal); Project administration (equal); Resources (equal); Software (equal); Supervision (equal); Writing – review & editing (equal).

DATA AVAILABILITY

The data that support the findings of this study are available within the article and its supplementary material.

REFERENCES

[1] E. Almeida, T. C. Diamantino, and O. de Sousa, "Marine paints: The particular case of antifouling paints," Prog. Org. Coat. **59**, 2–20 (2007).
[2] S. Pan, R. Guo, M. Björnmalm, J. J. Richardson, L. Li, C. Peng, N. Bertleff-Zieschang, W. Xu, J. Jiang, and F. Caruso, "Coatings super-repellent to ultralow surface tension liquids," Nat. Mater. **17**, 1040–1047 (2018).
[3] J. Xiao, "How lithium dendrites form in liquid batteries," Science **366**, 426–427 (2019).
[4] M. Wang and Z. Feng, "Interfacial processes in electrochemical energy systems," Chem. Commun. **57**, 10453–10468 (2021).
[5] E. Arzt, H. Quan, R. M. McMeeking, and R. Hensel, "Functional surface microstructures inspired by nature—From adhesion and wetting principles to sustainable new devices," Prog. Mater. Sci. **120**, 100823 (2021).
[6] A. F. Demirörs, S. Aykut, S. Ganzeboom, Y. A. Meier, and E. Poloni, "Programmable droplet manipulation and wetting with soft magnetic carpets," Proc. Natl. Acad. Sci. U. S. A. **118**, e2111291118 (2021).
[7] T.-H. Shen, L. Spillane, J. Peng, Y. Shao-Horn, and V. Tileli, "Switchable wetting of oxygen-evolving oxide catalysts," Nat. Catal. **5**, 30–36 (2022).
[8] P.-G. de Gennes, "Wetting: Statics and dynamics," Rev. Mod. Phys. **57**, 827 (1985).
[9] F. Wang, Y. Wu, and B. Nestler, "Wetting effect on patterned substrate," Adv. Mater. **35**, 2210745 (2023).
[10] T. D. Blake, "The physics of moving wetting lines," J. Colloid Interface Sci. **299**, 1–13 (2006).
[11] C. Huh and L. E. Scriven, "Hydrodynamic model of steady movement of a solid/liquid/fluid contact line," J. Colloid Interface Sci. **35**, 85–101 (1971).
[12] Y. Sui, H. Ding, and P. D. M. Spelt, "Numerical simulations of flows with moving contact lines," Annu. Rev. Fluid Mech. **46**, 97–119 (2014).
[13] C. W. Hirt and B. D. Nichols, "Volume of fluid (VOF) method for the dynamics of free boundaries," J. Comput. Phys. **39**, 201–225 (1981).
[14] M. Sussman, A. S. Almgren, J. B. Bell, P. Colella, L. H. Howell, and M. L. Welcome, "An adaptive level set approach for incompressible two-phase flows," J. Comput. Phys. **148**, 81–124 (1999).
[15] G. Tryggvason, B. Bunner, A. Esmaeeli, D. Juric, N. Al-Rawahi, W. Tauber, J. Han, S. Nas, and Y.-J. Jan, "A front-tracking method for the computations of multiphase flow," J. Comput. Phys. **169**, 708–759 (2001).
[16] A. J. Briant, "Lattice Boltzmann simulations of contact line motion in a liquid-gas system," Philos. Trans. R. Soc. London, Ser. A **360**, 485–495 (2002).
[17] A. J. Briant, A. J. Wagner, and J. M. Yeomans, "Lattice Boltzmann simulations of contact line motion. I. Liquid-gas systems," Phys. Rev. E **69**, 031602 (2004).
[18] A. J. Briant and J. M. Yeomans, "Lattice Boltzmann simulations of contact line motion. II. Binary fluids," Phys. Rev. E **69**, 031603 (2004).
[19] D. Jacqmin, "Contact-line dynamics of a diffuse fluid interface," J. Fluid Mech. **402**, 57–88 (2000).
[20] J. W. Cahn and J. E. Hilliard, "Free energy of a nonuniform system. I. Interfacial free energy," J. Chem. Phys. **28**, 258–267 (1958).
[21] F. Wang, H. Zhang, Y. Wu, and B. Nestler, "A thermodynamically consistent diffuse interface model for the wetting phenomenon of miscible and immiscible ternary fluids," J. Fluid Mech. **970**, A17 (2023).
[22] J. W. Cahn, "Critical point wetting," J. Chem. Phys. **66**, 3667–3672 (1977).
[23] W. Villanueva and G. Amberg, "Some generic capillary-driven flows," Int. J. Multiphase Flow **32**, 1072–1086 (2006).

[24]V. V. Khatavkar, P. D. Anderson, and H. E. H. Meijer, "Capillary spreading of a droplet in the partially wetting regime using a diffuse-interface model," J. Fluid Mech. **572**, 367–387 (2007).
[25]L. Liu and T. Lee, "Wall free energy based polynomial boundary conditions for non-ideal gas lattice Boltzmann equation," Int. J. Mod. Phys. C **20**, 1749–1768 (2009).
[26]P. Yue, C. Zhou, and J. J. Feng, "Sharp-interface limit of the Cahn–Hilliard model for moving contact lines," J. Fluid Mech. **645**, 279–294 (2010).
[27]A. Carlson, M. Do-Quang, and G. Amberg, "Droplet dynamics in a bifurcating channel," Int. J. Multiphase Flow **36**, 397–405 (2010).
[28]H. S. Wiklund, S. B. Lindström, and T. Uesaka, "Boundary condition considerations in lattice Boltzmann formulations of wetting binary fluids," Comput. Phys. Commun. **182**, 2192–2200 (2011).
[29]A. Carlson, M. Do-Quang, and G. Amberg, "Dissipation in rapid dynamic wetting," J. Fluid Mech. **682**, 213–240 (2011).
[30]H. Liang, H. Liu, Z. Chai, and B. Shi, "Lattice Boltzmann method for contact-line motion of binary fluids with high density ratio," Phys. Rev. E **99**, 063306 (2019).
[31]P. Yue, "Thermodynamically consistent phase-field modelling of contact angle hysteresis," J. Fluid Mech. **899**, A15 (2020).
[32]M. Ben Said, M. Selzer, B. Nestler, D. Braun, C. Greiner, and H. Garcke, "A phase-field approach for wetting phenomena of multiphase droplets on solid surfaces," Langmuir **30**, 4033–4039 (2014).
[33]Y. Wu, F. Wang, W. Huang, M. Selzer, and B. Nestler, "Capillary adsorption of droplets into a funnel-like structure," Phys. Rev. Fluids **7**, 054004 (2022).
[34]F. Oktasendra, A. Jusufi, A. R. Konicek, M. S. Yeganeh, J. R. Panter, and H. Kusumaatmaja, "Phase field simulation of liquid filling on grooved surfaces for complete, partial, and pseudo-partial wetting cases," J. Chem. Phys. **158**, 204501 (2023).
[35]J. Zhang and D. Y. Kwok, "Lattice Boltzmann study on the contact angle and contact line dynamics of liquid–vapor interfaces," Langmuir **20**, 8137–8141 (2004).
[36]K. Connington and T. Lee, "Lattice Boltzmann simulations of forced wetting transitions of drops on superhydrophobic surfaces," J. Comput. Phys. **250**, 601–615 (2013).
[37]T. Qian, X.-P. Wang, and P. Sheng, "A variational approach to moving contact line hydrodynamics," J. Fluid Mech. **564**, 333–360 (2006).
[38]H. Ding and P. D. M. Spelt, "Wetting condition in diffuse interface simulations of contact line motion," Phys. Rev. E **75**, 046708 (2007).
[39]F. Wang and B. Nestler, "Wetting transition and phase separation on flat substrates and in porous structures," J. Chem. Phys. **154**, 094704 (2021).
[40]B. Nestler, F. Wendler, M. Selzer, B. Stinner, and H. Garcke, "Phase-field model for multiphase systems with preserved volume fractions," Phys. Rev. E **78**, 011604 (2008).
[41]J.-J. Huang, H. Huang, and X. Wang, "Wetting boundary conditions in numerical simulation of binary fluids by using phase-field method: Some comparative studies and new development," Int. J. Numer. Methods Fluids **77**, 123–158 (2015).
[42]R. Huang, Q. Li, and N. A. Adams, "Surface thermodynamics and wetting condition in the multiphase lattice Boltzmann model with self-tuning equation of state," J. Fluid Mech. **940**, A46 (2022).
[43]M. Gao and X.-P. Wang, "An efficient scheme for a phase field model for the moving contact line problem with variable density and viscosity," J. Comput. Phys. **272**, 704–718 (2014).
[44]L. Luo, X.-P. Wang, and X.-C. Cai, "An efficient finite element method for simulation of droplet spreading on a topologically rough surface," J. Comput. Phys. **349**, 233–252 (2017).
[45]J. J. Huang, C. Shu, J. J. Feng, and Y. T. Chew, "A phase-field-based hybrid lattice-Boltzmann finite-volume method and its application to simulate droplet motion under electrowetting control," J. Adhes. Sci. Technol. **26**, 1825–1851 (2012).
[46]J. D. van der Waals, "The thermodynamic theory of capillarity under the hypothesis of a continuous variation of density," J. Stat. Phys. **20**, 200–244 (1979).
[47]P. Yue and J. J. Feng, "Wall energy relaxation in the Cahn–Hilliard model for moving contact lines," Phys. Fluids **23**, 012106 (2011).
[48]A. Carlson, M. Do-Quang, and G. Amberg, "Modeling of dynamic wetting far from equilibrium," Phys. Fluids **21**, 121701 (2009).
[49]X. Xu and X. Wang, "Derivation of the Wenzel and Cassie equations from a phase field model for two phase flow on rough surface," SIAM J. Appl. Math. **70**, 2929–2941 (2010).
[50]H. K. Hardy, "A 'sub-regular' solution model and its application to some binary alloy systems," Acta Metall. **1**, 202–209 (1953).
[51]E. A. Guggenheim, "The theoretical basis of Raoult's law," Trans. Faraday Soc. **33**, 151–156 (1937).